# The Influence of Microphysical Cloud Parameterizations on Microwave Brightness Temperatures

G.M. Skofronick-Jackson
University of Maryland, Baltimore County
Goddard Earth Sciences and Technology Center
Seabrook, Maryland 20706
and
A.J. Gasiewski
NOAA Environmental Technology Laboratory
R/E/ET1 Room A353
325 Broadway
Boulder, Colorado 80303
and
James R. Wang
Microwave Sensors Branch
NASA Goddard, Code 975
Greenbelt, MD 20771

To be submitted for publication in:
Journal of Applied Meteorology
December 6, 2000

# Abstract

The microphysical parameterization of clouds and raincells plays a central role in atmospheric forward radiative transfer models used in calculating passive microwave brightness temperatures. The absorption and scattering properties of a hydrometeor-laden atmosphere are governed by particle phase, size distribution, aggregate density, shape, and dielectric constant. This study identifies the sensitivity of brightness temperatures with respect to the microphysical cloud parameterization. Cloud parameterizations for wideband (6–410 GHz) observations of baseline brightness temperatures were studied for four evolutionary stages of an oceanic convective storm using a five-phase hydrometeor model in a planar-stratified scattering-based radiative transfer model. Five other microphysical cloud parameterizations were compared to the baseline calculations to evaluate brightness temperature sensitivity to gross changes in the hydrometeor size distributions and the ice-air-water ratios in the frozen or partly frozen phase. The comparison shows that enlarging the rain drop size or adding water to the partly frozen hydrometeor mix warms brightness temperatures by up to 55 K at 6 GHz. The cooling signature caused by ice scattering intensifies with increasing ice concentrations and at higher frequencies. An additional comparison to measured Convection and Moisture Experiment (CAMEX-3) brightness temperatures shows that in general all but two parameterizations produce calculated $T_B$'s that fall within the observed clear-air minima and maxima. The exceptions are for parameterizations that enhance the scattering characteristics of frozen hydrometeors.

# 1. Introduction

Over the past four decades, significant effort has been devoted to understanding the microphysical cloud characteristics of convective storms (e.g., Joss et al. 1968; Adler et al. 1991; Rutledge and Hobbs 1984). The microphysics of clouds is of considerable interest in a wide range of interdisciplinary studies. These studies include improving global climate models for understanding climate variability, investigating the role of hydrometers in lightning generation, examining chemical interactions and rain evolution in clouds for pollution research, studying radar and lidar remote sensing applications, and developing precipitation parameter retrievals from satellite-based passive microwave imagery.

Of interest here is improving our understanding of the relationships between the microphysics of hydrometeors in a convective storm and the upwelling microwave brightness temperatures for the purposes of rain rate and precipitation parameter retrieval. A comprehensive understanding of these relationships is hindered by the lack of accurate and sufficiently detailed atmospheric microphysical profile truth (Smith et al. 1992; Evans et al. 1995). Difficulties in obtaining microphysical cloud profile truth for convective systems stem from limitations in remotely sensed measurements, aircraft sampling capabilities, and the extremely inhomogeneous and complex nature of convection (Kuo et al. 1997; Landsburg 1981). The dynamics of convection complicate the *in situ* measurements of hydrometeor size, shape, total water content and the ice-air-water ratio, and Nyquist spatial and temporal sampling of these quantities remains a formidable challenge.

A microphysical cloud parameterization requires specifying the size distributions and ice-air-water ratios for each hydrometeor type at each atmospheric level along with vertical profiles of temperature, relative humidity, and pressure. Parameterizations have been developed using knowledge from *in situ*, radar, and lidar observations as well as statistics from physical models of particle growth and coalescence. Early cloud parameterizations (e.g., Wilheit et al. 1977) allowed for a uniform rain layer and separate cloud water layer with no ice particles. Later models added an ice layer (e.g., Wilheit et al. 1982; Weinman and Davies 1978; Gasiewski and Staelin 1990; Bauer and Schluessel 1993).

Contemporary microphysical cloud parameterizations allow for multiple liquid and ice phases (e.g., Adler et al. 1991; Smith et al. 1992; Skofronick-Jackson and Gasiewski 1995; Ferrier et al. 1995). Several research studies have indicated that five hydrometeor phases adequately represent a convective storm (McCumber et al. 1991; Evans et al. 1995) from the standpoint of passive microwave signatures. The five hydrometeor phases are generally classified as cloud water, rain drops, cloud ice, snow (or ice aggregates), and graupel (including hail). The rain drops are commonly modeled by the Marshall and Palmer (1948) (MP) size distribution. However there appear to be no universally accepted size distributions or ice-air-water ratios for the other four hydrometeor types (Kuo et al. 1997). While similar, the microphysical parameterizations used by radiative transfer modelers are generally accurate for only specific storm occurrences.

As satellite passive microwave sensing of rain rate and other precipitation parameters (e.g., celltop altitude, see Gasiewski and Staelin (1989)) matures it is important to understand the impact of the various common hydrometeor parameterizations on the upwelling microwave brightness. Accordingly, the purpose of this work is to study the sensitivity of computed microwave brightness temperatures to changes in the microphysical parameters. The analysis of these changes is facilitated using wideband microwave aircraft data. Since identifying the best parameterization requires detailed collocated and coincident *in situ*, radar, and radiometer observations, we focus on identifying a plausible class of parameterizations rather than the best single parameterization. Indeed, cloud parameterizations are case specific. The work of Prasad et al. (1995) and Meneghini et al. (1997) are two examples where parameterizations that best match case-specific radiometer observations have been determined. Even though an optimal parameterization cannot be identified in this study, inappropriate and unrealistic parameterizations can be identified.

In studying microphysical cloud parameterizations and their effect on computed brightness temperatures, a planar-stratified atmosphere and a mid-latitude oceanic surface are assumed. The simple planar model is adequate for all but the most localized cumuluform convection. The highly reflective oceanic background provides greater sensitivity to hydrometeor scattering and absorption than would a land background, and thus represents the more conservative of the two backgrounds. For comparison purposes, four cloud profiles are selected to represent the early cumulus, evolving, mature and dissipating stages of a convective storm. Six microphysical cloud parameterizations were selected for use in evaluating brightness temperature sensitivities to the hydrometeor size parameters, and frozen particle ice-air-water ratios. A five-hydrometeor-phase (cloud water, rain, cloud ice, dry snow, and dry graupel) parameterization is considered to be the baseline case (parameterization #1). This case uses the MP distribution for rain, modified MP distributions for snow and graupel, and monodispersions for cloud water and cloud ice. The ice-air-water ratio for snow and graupel are 10%-90%-0% and 40%-60%-0%, respectively. The other parameterizations are obtained using the following variations: (2) the Joss et al. (1968) thunderstorm rain drop size distribution (instead of MP), (3) the Sekhon-Srivastava (SS) size distribution for snow and graupel (instead of the modified MP size distribution), (4) a doubling of the percentage of ice in the ice-air-water ratios of snow and graupel to 20%-80%-0% and 80%-20%-0%, respectively, (5) the addition of a temperature-dependent amount of water to the snow and graupel components, and (6) a simple two-phase model that allows for only rain and ice hydrometeors. Brightness temperatures at twelve frequencies (6.0, 10.69, 18.7, 23.8, 36.5, 89.0, 150.0, 183.31+7.0, 220.0, 325+8.0, 340.0, and 410.0 GHz) were computed for each of the four cloud stages and six parameterizations using the planar-stratified scattering-based radiative transfer model of Gasiewski and Staelin (1990). We discuss herein the variations in brightness temperature values when the microphysical cloud parameterization is changed in the radiative transfer calculations.

While convective storms under different prevailing conditions (e.g., tropical, mid-latitude, maritime, or continental) have differing hydrometeor characteristics, this study nonetheless identifies several issues. First, in order to select the proper parameterization for any specific condition, one requires a set of detailed atmospheric truth profiles along with a collocated and coincident set of brightness temperature observations. Second, the choice of dielectric mixing theory models for mixed-phase hydrometeors greatly impacts the high frequency channels. Third, we show the sensitive relationship between the brightness temperature and the underlying rain rate. In identifying these issues we first briefly describe the radiative transfer model and calculations, including the ocean surface and top-of-atmosphere conditions. Dielectric mixing theory for heterogeneous snow and graupel particles is outlined. Section 3 details the six microphysical cloud parameterizations. The absorption and scattering coefficients for selected parameterizations are also presented in this section. The comparison among the six parameterizations (Section 4) and to the aircraft data (Section 5) is described with a summary in Section 6.

## 2. Radiative Transfer Model

The planar-stratified radiative transfer (RT) model developed by Gasiewski and Staelin (1990) is used to compute the upwelling brightness temperature ($T_B$) vectors.

In this iterative model, scattering is considered to be a perturbation to the clear-air $T_B$ solution (Gasiewski and Staelin 1990; Liou 1980). To simplify the analysis the brightness temperature observation angle was assumed to be nadir ($\theta = 0°$) and horizontally-finite cloud structures were not considered. The aggregate absorption and scattering coefficients of the atmosphere ($\mathcal{K}_a$, $\mathcal{K}_s$, respectively) are obtained from the atmospheric state at each level. The aggregate absorption and scattering coefficients are equal to the algebraic sum of all the individual hydrometeor absorption and scattering coefficients. The algebraic sum can be used because the hydrometeors are randomly distributed and thus scatter incoherently. The aggregate coefficients are given by:

$$\mathcal{K}_a = \kappa_{O_2} + \kappa_{H_2O} + \sum_{h=1}^{H} \kappa_{a_h} \tag{1}$$

$$\mathcal{K}_s = \sum_{h=1}^{H} \kappa_{s_h} . \tag{2}$$

where $\kappa_{a_h}$ and $\kappa_{s_h}$ denote the absorption and scattering contributed by an individual atmospheric constituent or hydrometeor type $h$, and $H$ is the number of hydrometeor types modeled.

The individual absorption ($\kappa_{a_h}$) and scattering ($\kappa_{s_h}$) coefficients are governed by the size distribution, density, shape, and dielectric constant of both gases and hydrometeors. Water vapor and oxygen absorb electromagnetic radiation as described by Liebe (1987) and Rosenkranz (1988), and denoted by $\kappa_{a_{H_2O}}$ and $\kappa_{a_{O_2}}$ (respectively). Polydispersive particle size distributions are assumed for the cloud particles. The absorption and scattering coefficients are determined by integrating the Mie efficiencies over the polydispersive size distribution (Gasiewski 1993). In practice, simplified numerical calculations are available using Rayleigh theory (Wiscombe 1980) for electrically small particles, (i.e., $\langle D \rangle \ll \frac{0.1\lambda}{\pi}$) or the reformulated Mie equations from Diermendjian (1969) for electrically large particles.

The particle size distribution (PSD), or number density of particles within the diameter range $D$ to $D + \mathrm{d}D$, is modeled by a decaying inverse exponential function:

$$N_h(D) = N_{h_0} e^{-\Lambda_h D} \quad (\mathrm{cm}^{-4}) \tag{3}$$

where (Rutledge and Hobbs 1984)

$$\Lambda_h = [\pi \rho_h N_{h_0} / M_h]^{0.25} \quad (\mathrm{cm}^{-1}) = \langle D \rangle^{-1}. \tag{4}$$

In the above, $M_h$ is the partial density in g/cm$^3$ of hydrometeor type $h$, $\rho_h$ is the average intrinsic density in g/cm$^3$, $N_{h_0}$ in cm$^{-4}$ is a multiplier, and $\langle D \rangle$ is the average hydrometeor diameter for the ensemble. The subscript $h$ is used to distinguish among the various classes of hydrometeors (e.g., $\rho_w$, $\rho_r$, $\rho_i$, $\rho_s$, and $\rho_g$ for the intrinsic density of cloud water, rain, ice, snow, and graupel, respectively). For large particle diameters (i.e., greater than $\sim$0.5 mm in diameter and for frequencies between $\sim$10 and $\sim$300 GHz the liquid scattering coefficient $\kappa_s$ is slightly greater than the liquid absorption coefficient $\kappa_a$ (Gasiewski 1993), otherwise liquid absorption is greater than liquid scattering. Ice scattering dominates ice absorption for all microwave frequencies and particle sizes. The relationship between the aggregate scattering coefficient $\mathcal{K}_s$ and aggregate absorption coefficient $\mathcal{K}_a$ can be used to indicate if radiative cooling from scattering or warming from absorption will occur.

The complex dielectric constant needed to compute $\mathcal{K}_s$ and $\mathcal{K}_a$ is a function of frequency, temperature, and the constituent materials of the hydrometeor (e.g., water, ice, or a heterogeneous mixture of ice and air and/or water). Dielectric constants for liquid and homogeneous ice hydrometeors are easily obtained using available Debye relaxation formulae or tables (Lane and Saxton 1952; Warren 1984). In contrast, heterogeneous hydrometeors require the use of dielectric mixing theory. A dielectric mixing theory appropriate for precipitation-sized particles is the explicit Maxwell-Garnett formula (Bohren and Battan 1980) which is equivalent to the implicit Rayleigh mixing formula. Although mixing theories exist for ellipsoidal particles or multilayer spheroidal inclusions (Sihvola 1989), the use of such detailed models warrants separate study. The Maxwell-Garnett mixing theory states that given a host material with dielectric constant $\epsilon_0$ and dielectric inclusions $\epsilon_1$ with size $l \ll \lambda$ the effective dielectric constant is:

$$\epsilon_{eff} = \epsilon_0 \left[ 1.0 + \frac{3.0v\left(\frac{\epsilon_1-\epsilon_0}{\epsilon_1+2\epsilon_0}\right)}{1 - v\left(\frac{\epsilon_1-\epsilon_0}{\epsilon_1+2\epsilon_0}\right)} \right] \tag{5}$$

where $v$ is the volume fraction of the inclusions (Sihvola 1989). In this work we assume temperature dependent ice-air-water ratios.

The above mixing formula (5) breaks down at high frequencies where the wavelength is smaller than the size of the inclusions. A more appropriate dielectric mixing theory for high frequencies is that of Goedecke and O'Brien (1988), however such a computationally-intensive mixing theory is unnecessary due to constraints on the inclusion size. For large graupel we may have, e.g., $\langle D \rangle = 4$ mm. If we assume that $l \leq \langle D \rangle/4$, then we can satisfy $l \ll \lambda$ for all but the highest frequencies of concern and the largest particles. Moreover, since the higher frequencies are unable to probe to the cloud depths where the largest particles exist, the mixing theory in (6) as used in this study is valid.

# 3. Microphysical Cloud Parameterizations

As RT cloud models developed, the complexity of the cloud parameterizations increased from two-phases (e.g., Wilheit et al. 1982; Gasiewski and Staelin 1990; Bauer and Schluessel 1993) that included only liquid and ice spheres to multiple liquid and ice phases (e.g., Adler et al. 1991; Smith et al. 1992; Evans et al. 1995) and non-spherical ice particles (Evans et al. 1995). Within the class of spherical particle models the multiple natural phases of liquid and ice hydrometeors are well represented by a five-phase parameterization that allows for non-precipitating cloud water, rain, non-precipitating ice, dry snow, and dry graupel. The last of these constituents is essentially hail with entrained air (Rutledge and Hobbs 1984; Adler et al. 1991). While the use of spherically symmetric particles is somewhat idealized, this simplification allows the important effects of particle size distribution and dielectric constitution to be considered separately from that of aspherical particle orientation.

We assume that rain, snow, and graupel hydrometeors have the exponential size distributions of Rutledge and Hobbs (1984) given in Eqns. 3 and 4 with parameters $N_{0_h}$ and $\rho_h$ given in Table 1. The ice-air-water ratios for cloud water, rain, cloud ice, snow, and graupel are 0-0-100%, 0-0-100%, 100-0-0%, 10-90-0%, and 40-50-0% respectively. The cloud particles have a fixed mean diameter of $\langle D \rangle = 0.002$ cm $= (\Lambda)^{-1}$ and thus are small enough to advect with the airflow. The parameters $N_w$ and $N_i$ (the number of density particles) vary to account for the differing mass densities $M_w$ and $M_i$.

The six microphysical parameterizations investigated in this study are presented in Table 2. All parameterizations use the same underlying storm profile data. The previously described five-phase model with dry snow and dry graupel is considered the baseline case (case 1) because of its general acceptance and use elsewhere (Adler et al. 1991; McCumber et al. 1991). Furthermore, brightness temperature values obtained with this five phase model are corroborated by low frequency aircraft observations (Skofronick-Jackson and Gasiewski 1995). Parameterizations 2-5 are identical to the five-phase baseline case, except for the modifications described below. Parameterizations 2 and 3 have modified particle size distributions as follows: For parameterization 2 we use the (Joss et al. 1968) thunderstorm size distribution for rain, and for parameterization 3 we use the Sekhon and Srivastava (1970, SS) size distribution for the dry snow and graupel. The Joss thunderstorm size distribution favors fewer small-sized particles and more large-sized particles than the MP size distribution. For parameterization 3, ice particles are assumed to be solid spheres with an SS distribution: $N_i = 6.4 \times 10^{-3} M_i^{-1.09}$ (cm$^{-4}$) and $\Lambda_i = 11.9 M_i^{-0.52}$ (cm$^{-1}$). The SS size distribution is an equivalent liquid-sphere size distribution for snowflakes near the ground that yields precipitation rates that are consistent with measured snowflake terminal velocities (Sekhon and Srivastava 1970). The SS size distribution leads to more smaller-sized particles than the modified MP distributions of the five-phase case.

There are two parameterizations (4 and 5) with varied air-ice-water ratios in snow and graupel. Parameterization 4 doubles the percentage of snow and graupel such that $\rho_s = 0.2$ g/m$^3$ and $\rho_g = 0.8$ g/m$^3$ (i.e., ice-air-water ratios of 20%–80%–0% and 80%–20%–0%, respectively) making the snow and graupel hydrometeors more typical of aggregates and hail (McCumber et al. 1991). Doubling the ice percentage will increase the scattering coefficient with respect to parameterization 1. Parameterization 5 adds a wetness percentage ($W$) to the snow and graupel particles as a function of the atmospheric temperature (in K):

$$W(\%) = \begin{cases} 0.0 & \text{for } T \leq -15^\circ C \\ T - 258.15 & \text{for } -15^\circ C < T \leq 0^\circ C \\ 15.0 & \text{for } T > 0^\circ C \end{cases} \tag{6}$$

The ice-air-water ratios are adjusted by removing $W$ from the air percentage and adding the same amount to the water percentage. The Maxwell-Garnett dielectric mixing formula is applied twice, once with ice inclusions in an air matrix and then with water inclusions in the air-ice matrix. Adding water will increase the absorption coefficient and cause brightness temperature warming. This "wet" parameterization models snow and graupel absorption within the melting layer. Melting effects are the basis for the brightband near the melting level in radar meteorology.

Finally parameterization 6 lumps the ice, snow, and graupel into solid spherical frozen hydrometeors with the SS size distribution. Similarly, the rain and cloud water are combined to form a single rain phase with a MP distribution. This parameterization is included to provide intercomparison with the two-phase parameterizations commonly used in many previous studies.

The microphysical cloud data used in the six cloud parameterizations is from the Goddard Cloud Ensemble (GCE) simulation of a convective tropical squall (Adler et al.

1991; Tao and Simpson 1993). The microphysical information at each point in a storm frame includes height, temperature, relative humidity, and the partial density $M_h$ for cloud water, rain, ice, snow, and graupel (Tao and Simpson 1993). The vertical profiles extend from the ocean surface to between 12 and 20 km and have a varying altitude spacing that is smaller ($< 1$ km) where convective clouds exist. At the lower boundary of the GCE profile data a calm ocean surface at 18°C is assumed. A calm surface is defined by a wind speed $\leq 7$ m/s causing no significant surface roughness. The boundary condition at the top of the atmosphere is the cosmic background temperature of 2.73 K.

# 4. Comparisons

Comparisons focus on four evolutionary profiles from the three-dimensional GCE data. Each of the four evolutionary stages provides a distinct "snapshot" of the storm. The cumulus stage (C) (Fig. 1a) has low rain and graupel densities, but significant suspended cloud water. The large cloud water concentration is representative of a storm early in its evolution. The evolving stage (E) (Fig. 1b) has much rain but little ice or graupel and represents a storm further in its early development. The mature stage (M) (Fig. 1c) has high rain densities at low altitudes ($< 4$ km) and high graupel densities between 4 and 10 km. This profile is representative of a storm at peak convection (Adler et al. 1991). Finally, the dissipating stage (D) (Fig. 1d) has moderate low-altitude rain and significant graupel at mid-level altitudes. It is representative of a weakening post-convective storm with a developing anvil region. The GCE temperature and relative humidity profiles for the four stages are shown in Fig. 2. The temperature profiles show little variation, while the relative humidity profiles show variation similar to the cloud water and rain profiles. The rain rates and integrated ice contents of the four storm stages are provided in Table 3.

Nadir brightness temperatures at twelve microwave frequencies (6.0, 10.69, 18.7, 23.8, 36.5, 89, 150.0, 183.310+7.0, 220.0, 325+8.0, 340.0, and 410.0 GHz) were computed for each of the four stages and six microphysical parameterizations. A comparison of the computed brightness temperature values for each of the frequencies follows in Figures 3 a - 3 l. The plot for each frequency presents the $T_B$ values as a function of the parameterizations. The symbols $\times$, $\square$, $\circ$, $\triangle$ indicate storm stage C (cumulus), E (evolving), M (mature), and D (dissipating), respectively. The $T_B$ values are presented as perturbations from clear air values. Not including the data to the right of the dotted line, (to be discussed in Section 5), two tables have been developed to intercompare the parameterizations, storm stages, and $T_B$ values at each frequency. Table 4 details the $T_B$ variations for each frequency over the six microphysical parameterizations, while Table 5 provides a summary of the effects of each parameterization for the four stages. Tables 4 and 5 use parameterization 1 as the reference. A brief textual summary of Fig. 3 and Tables 4 and 5 follows.

A summary of $T_B$ responses from low to high frequency follows from Fig. 3. At 6 GHz a warming response due to absorption from only the highest densities and thus the largest rain drops is expected. The absorptive signature of rain at 10.69 GHz is significant. Liquid scattering (cooling) occurs when the size of the rain drop exceeds 0.5 mm or the rain rate exceeds ~30 mm/hr (Gasiewski 1993). Thus the bulk liquid scattering coefficient at 10 GHz is only weakly dependent on the hydrometeor size. Ice scattering should not be a prominent contributor to the signature at 10 GHz unless the density of ice is extremely high. At 18 GHz, scattering from only the largest ice particles begins to cause cooling (Adler et al. 1991; Smith et al. 1992). The 23.8 GHz water vapor channel is very sensitive to cloud water and the ice scattering signature increases. Thus, the stage with the largest amount of cloud water and the fewest frozen hydrometeors (stage C) shows the warmest $T_B$ values at 23.8 GHz across all parameterizations. At 36.5 GHz the effects of ice scattering are considerable and start to cancel the absorptive warming due to rain. For the 89 GHz channel, scattering dominates the spectral signature while liquid water absorption plays only a minor role. Above 89 GHz, the scattering signature is stronger than the absorptive warming signature and all $T_B$ values are below the clear air $T_B$ values (negative perturbation values). Above 220 GHz, the $T_B$ variability among all six parameterizations and four stages is reduced. The compression is caused by an increasing sensitivity to hydrometeor size and increasing cloud-top opacity as wavelength decreases. This sensitivity can saturate the response to cloud and hydrometeor particles at these higher frequencies. The large opacity also precludes probing into the highly variable lower levels of the storm. The cloud top opacity also explains why the $T_B$ variations of the early cumulus profile (stage C, with its limited ice), are not strongly compressed.

Table 4 identifies changes of more than 5 K with respect to parameterization 1. This table shows that the Joss PSD (parameterization 2) only affects frequencies at or below 36.5 GHz. The Joss parameterization warms all storm stages at 6 GHz and warms the 10 and 18 GHz channels when the rain rate is low (stages C and D). The Joss PSD cools $T_B$ values at the higher frequencies when the rain rate is high since it produces larger drops that increase scattering.

The SS PSD (parameterization 3) produces warmer $T_B$ values for frequencies at and above 18.7 GHz because the SS PSD generates smaller snow and graupel particles than does parameterization 1. At the lower frequencies only storm stages with significant ice are warmed (stages E, M, D). However at higher frequencies ($\geq$ 150 GHz), the SS PSD does not change the $T_B$ values of stage M because ice scattering reaches saturation regardless of the ice PSD.

On the other hand, parameterization 4 causes cooling at all frequencies above 6.0 GHz. The increased ice percentage in the snow and graupel particles generates increased scattering. There is less than a 5 K response for storm stage C for frequencies below 36.5 GHz because stage C has little snow and graupel. At 410 GHz saturation results in a minimal variation (< 5 K) for stage M.

For parameterization 5 the snow and graupel have a variable liquid water fraction, and a general warming of the $T_B$ values occurs. There is a single incidence of a decreased $T_B$ value at 10 GHz. This is likely due to the fact that the "melted" snow and graupel particles appear to be large rain drops at 10 GHz—large enough to cause some scattering. Since the higher frequencies respond to the high-altitude frozen hydrometeors, there is little change in the high frequency $T_B$ values from parameterization 1 to parameterization 5.

Table 5 reinforces the data in Table 4 while providing details of the relationships between storm stage and parameterization. Associated with Table 5 is a coded summary detailing the $T_B$ changes for each storm type as a function of parameterization.

# 5. Aircraft Intercomparisons

In Fig. 3, nadir $T_B$ perturbations from high-altitude aircraft observations are plotted to the right of the dotted line for frequencies where observed data is available. The observations are from the Millimeter-wave Imaging Radiometer (MIR) (Racette et al. 1996) and the Advanced Microwave Precipitation Radiometer (AMPR) (Spencer et al. 1994) onboard the NASA ER-2. The MIR observed at 89, 150, 183.31±1, ±3, ±7, 220, and 340 GHz, while the AMPR observed at 10.7, 19.35, 37 and 85.5 GHz. Observations are obtained during the CAMEX-3 experiment (Geerts et al. 2000) on 26 August 1998 and 17 September 1998. The observations are roughly categorized into cumulus, evolving, mature, and dissipating stages. The observed $T_B$ minimum and maximum perturbations are indicated with matching cloud stage symbols and a line joining the minima and maxima.

Several features of the observed versus computed data are enumerated. First, most of the calculations are within the minimum and maximum observed values indicating that the parameterizations are appropriate in most cases. Second, for 220 and 340 GHz the calculated values are well within the observed minima and maxima for all parameterizations. This observation suggests increasing the complexity of frozen hydrometeor PSDs and their air-ice-water mixtures in simulated cloud profiles and thus the resulting $T_B$ ranges. Next note that for parameterization 4 the calculated $T_B$ values are too cool for most of the stages and frequencies between 18 and 89 GHz. This observation implies that parameterization 4 produces too much ice scattering at the low and middle frequencies. Similarly, the two-phase model (parameterization #6) produces $T_B$ values warmer than the maxima of the 10 and 18 GHz observations for the cumulus and evolving stages and cooler than the minima for most of the stages and the mid-frequencies (18–150 GHz). A plausible explanation is that combining the rain and cloud water increases absorptive warming, while combining the cloud ice, snow, and graupel densities increases scattering and cooling. Since parameterization 6 is consistently outside the minima and maxima of the observations we conclude that it is not as applicable as the others for the cloud conditions observed during CAMEX. Finally, there are several individual stages and frequencies wherein the computed $T_B$ do not fall within the observed minima and maxima, in particular: at 10 GHz for stage E; at 36 GHz for stages M and D; and at 89 GHz for stages E and D. These inconsistencies could mean that the observation stages were inadequately categorized into cumulus, evolving, mature, and dissipating stages or that the parameterizations studied do not model the true microphysics of the observations. Only with detailed coincident $T_B$ observations and *in situ* PSD measurements can some of the inconsistencies be understood.

# 6. Summary

An investigation into how microphysical cloud parameterizations affect calculated oceanic microwave brightness temperature values was presented. Brightness temperatures at twelve frequencies between 6.0 and 410.0 GHz were computed for four storm stages obtained from the simulated GCE data set of Tao and Simpson (1989). The four profiles used in the comparison represent a convective storm in its early cumulus, evolving, mature, and dissipating stages.

The densities of the five hydrometeor types of the GCE data were converted into six different microphysical cloud parameterizations. The parameterizations were designed to evaluate brightness temperature sensitivity to particle size distributions and ice-air-water ratios. A comparison among the six parameterizations, four convective storm stages, and twelve frequencies was performed. A five hydrometeor-phase parameterization (Adler et al. 1991; Skofronick-Jackson and Gasiewski 1995) was considered as the baseline case.

The comparisons generally showed that increasing the emphasis of water or rain warmed the brightness temperatures. When the size distribution of rain was changed to that of the Joss *et al.* thunderstorm size distribution (which favors larger particle diameters), the $T_B$ values at 6 GHz were warmed by up to 55 K. At 18 and 23.8 GHz the larger-sized Joss particles initiate liquid scattering more so than the smaller-sized MP size distribution, resulting in a small $T_B$ cooling. From 10.69 GHz to 36.5 GHz, a transition from mostly absorptive (characterized by warmer $T_B$ values) to mostly scattering (characterized by cooler $T_B$ values) occurs. At stage C (the early cumulus profile), a change from having the coolest $T_B$ at 10.69 GHz for all parameterizations and pixels (because there is little absorptive warming) to having the warmest $T_B$ values at 36.5 GHz (because there is little scattering) occurs. Above 36.5 GHz changes in the rain drop size distribution initiated no differences in the $T_B$ values with respect to the five-phase model due to the strong scattering signatures of storm-top ice at these higher frequencies. Adding liquid water to the snow and graupel hydrometeors caused absorptive warming at the low and mid-frequencies.

From 89 GHz to 220 GHz the scattering signature is stronger than the absorptive warming signature. The comparison showed that the cooling signature due to ice scattering at higher frequencies was increased with larger ice concentrations. The ice concentration rose when additional ice was allocated to the ice-air-water ratio. Above 220 GHz the $T_B$ variability among all six parameterizations and four stages was reduced. The compression was caused by an increasing sensitivity to hydrometeor size as wavelength decreased. This increasing sensitivity caused an increased opacity at the higher frequencies.

Finally, a comparison of the calculated $T_B$ values with available observed $T_B$ values from the CAMEX-3 experiment showed acceptable agreement for most stages and parameterizations. Exceptions occurred for the doubled ice-ratio parameterization and the two-phase parameterization. These two parameterizations consistently yielded $T_B$ values outside the range of the observed minima and maxima, indicating that they are less physically realistic than the others. Another interesting feature is that the 220 and 340 GHz $T_B$ calculations are well within the minimums and maximums of the observations providing an argument for increasing the diversity and complexity of frozen hydrometeors in convective cloud profiles. (The parameterizations used herein do not provide enough diversity at these frequencies.) Finally, there are a few stages/parameterizations/frequencies whose calculations do not fall within the observed minima and maxima. These few inconsistent cases could mean that the clouds were inadequately categorized into cumulus, evolving, mature, and/or dissipating stages or that the parameterizations are not modeling the true cloud microphysics for all cases. A detailed coincident set of $T_B$ observations and *in situ* PSD measurements might be used to further refine cloud microphysical parameterizations.

Acknowledgments-This work has been supported by NASA Graduate Student Researchers Program (NGT-50903) and NASA Tropical Rainfall Measuring Mission (NAG5-7777). The authors thank Dr. J. Simpson, Dr. W.-K. Tao, and N. Prasad of the NASA/Goddard Space Flight Center for providing the Goddard Cumulus Ensemble (GCE) three-dimensional microphysical cloud data. The authors also thank the Global Hydrology Resource Center and Robbie Hood of the NASA Marshall Space Flight Center for providing the AMPR data. Finally we thank Will Manning of University of Maryland, Baltimore County for organizing the combined CAMEX data sets.

## )References

Adler, R. F., H.-Y. M. Yeh, N. Prasad, W.-K. Tao and J. Simpson, 1991: Microwave simulations of a tropical rainfall system with a three dimensional cloud model. *J. Appl. Meteor.*, **30**, 924–953.

Bauer, P. and P. Schluessel, 1993: Rainfall, total water, ice water, and water vapor over sea from polarized microwave simulations and special sensor microwave/imager data. *J. Geophys. Res.*, **98**, 20737–20759.

Bohren, C. F. and L. J. Battan, 1980: Radar backscattering by inhomogeneous precipitation particles. *J. Atmos. Sci.*, **37**, 1821–1827.

Diermendjian, D., 1969: *Electromagnetic Scattering on Spherical Polydispersions.* American Elsevier Publishing Company, Inc., New York.

Evans, K. F., J. Turk, T. Wong and G. L. Stephens, 1995: A bayesian approach to microwave precipitation profile retrieval. *J. Appl. Meteor.*, **34**, 260–279.

Ferrier, B. S., W.-K. Tao and J. Simpson, 1995: A double-moment multiple-phase four-class bulk ice scheme. part ii: Simulations of convective storms in different large-scale environments and comparisons with other bulk parameterizations. *J. Atmos. Sci.*, **52**(8), 1001–1033.

Gasiewski, A. J., 1993: Microwave radiative transfer in hydrometeors. in M. A. Janssen, editor, *Atmospheric Remote Sensing by Microwave Radiometry*, pp. 91–144. John Wiley and Sons, New York.

Gasiewski, A. J. and D. H. Staelin, 1989: Statistical precipitation cell parameter estimation using passive 118-ghz $O_2$ observations. *J. Geophys. Res.*, **94**(D15), 18367–18378.

Gasiewski, A. J. and D. H. Staelin, 1990: Numerical modeling of passive microwave $O_2$ observations over precipitation. *Radio Sci.*, **25**, 217–235.

Geerts, B., G. M. Heymsfield, L. Tian, J. B. Halverson, A. Guillory and M. I. Mejia, 2000: Hurricane Georges's landfall in the Dominican Republic: Detailed airborne doppler radar imagery. *Bull. Amer. Meteor. Soc.*, **81**(5), 999–1018.

Goedecke, G. H. and S. G. O'Brien, 1988: Scattering by irregular inhomogeneous particles via the digitized green's function algorithm. *Appl. Optics*, **27**(12).

Joss, J., J. C. Thams and A. Waldvogel, 1968: The variation of raindrop size distributions at Locarno. in *Proc. Int. Conf. on Cloud Physics*, pp. 369–373, Toronto, Canada.

Kuo, Y.-H., J. F. Bresch, M.-D. Cheng, J. Kain, D. B. Parsons, W.-K. Tao and D. L. Zhang, 1997: Meeting summary: Summary of a mini workshop on cumulus parameterization for mesoscale models. *Bulletin of the Amer. Meteor. Soc.*, **78**(3), 475–491.

Landsburg, H., 1981: Variability of the precipitation processes in time and space. in *ASTM Special Technical Publication, Conference: Sampling and Analysis of Rain*, pp. 3–9, Philadephia, PA. ASTM.

Lane, J. A. and J. A. Saxton, 1952: Dielectric dispersion in pure polar liquids at very high radio frequencies. *Proc. Roy. Soc. London*, **A213**, 400–408.

Liebe, H. J., 1987: A contribution to modeling atmospheric millimeter-wave properties. *Frequenz*, **41**, 31–36.

Liou, K.-N., 1980: *An Introduction to Atmospheric Radiation*. Academic Press, San Diego.

Marshall, J. S. and W. M. Palmer, 1948: The distribution of raindrops with size. *J. Meteor.*, **5**, 165–166.

McCumber, M., W.-K. Tao, J. Simpson, R. Penc and S.-T. Soong, 1991: Comparison of ice-phase microphysical parameterization schemes using numerical simulations of tropical convection. *J. Appl. Meteor.*, **30**, 985–1004.

Meneghini, R., H. Kumagai, J. R. Wang, T. Iguchi, and T. Kozu, 1997: Microphysical retrievals over stratiform rain using measurements from an airborne dual-wavelength radar-radiometer. *IEEE Trans. Geosci. Remote Sens.*, **35**, 487–506.

Prasad, N., H.-Y. M. Yeh, R. F. Adler and W.-K. Tao, 1995: Microwave and infrared simulations of an intense convective system and comparison with aircraft observations. *J. Appl. Meteor.*, **34**, 153–174.

Racette, P., R. F. Adler, J. R. Wang, A. J. Gasiewski, D. M. Jackson and D. S. Zacharias, 1996: An airborne millimeter-wave imaging radiometer for cloud, precipitation and atmospheric water vapor studies. *J. Atmos. Oceanic Technol.*, **13**, 610–619.

Rosenkranz, P. W., 1988: Interference coefficients for overlapping oxygen lines in air. *J. Quant. Spectrosc. Radiat. Transfer*, **39**, 287–297.

Rutledge, S. A. and P. Hobbs, 1984: The mesoscale and microscale structure and organization of clouds and precipitation in midlatitude cyclones. XII: A diagnostic modeling study of precipitation development in narrow cold-frontal rainbands. *J. Atmos. Sci.*, **41**, 2949–2972.

Sekhon, R. S. and R. Srivastava, 1970: Snow size spectra and radar reflectivity. *J. Atmos. Sci.*, **27**, 299–307.

Sihvola, A. H., 1989: Self-consistency aspects of dielectric mixing theories. *IEEE Trans. Geosci. Remote Sens.*, **27**, 403–415.

Skofronick-Jackson, G. M. and A. J. Gasiewski, 1995: Nonlinear statistical retrievals of ice content and rain rate from passive microwave observations of a simulated convective storm. *IEEE Trans. Geosci. Remote Sens.*, **33**(4), 957–970.

Smith, E. A., A. Mugnai, H. J. Cooper, G. J. Tripoli and X. Xiang, 1992: Foundations for statistical-physical precipitation retrieval from passive microwave satellite measurements. Part I: Brightness temperature properties of a time-dependent cloud-radiation model. *J. Appl. Meteor.*, **31**, 506–531.

Spencer, R. W., R. E. Hood, F. J. LaFontaine, E. A. Smith, R. Platt, J. Galliano, V. L. Griffin and E. Lobl, 1994: High-resolution imaging of rain systems with the advanced microwave precipitation radiometer. *J. Atmos. Oceanic Technol.*, **11**, 849–857.

Tao, W. K. and J. Simpson, 1989: Modelling study of a tropical squall-type convective line. *J. Atmos. Sci.*, **46**, 177–202.

Tao, W.-K. and J. Simpson, 1993: Goddard cumulus ensemble model. Part I: Model description. *Terrestrial, Atmos. and Oceanic Sciences*, **4**, 35–72.

Warren, S. G., 1984: Optical constants of ice from the ultraviolet to the microwave. *Appl. Optics*, **23**, 1206–1225.

Weinman, J. A. and R. Davies, 1978: Thermal microwave radiances from horizontally finite clouds of hydrometeors. *J. Geophys. Res.*, **83**(C6), 3099–3107.

Wilheit, T. T., A. T. C. Chang, J. L. King, E. B. Rodgers, R. A. Nieman, B. M. Krupp, A. S. Milman, J. S. Stratigos and H. Siddalingaiahi, 1982: Microwave radiometric observations near 19.35, 92 and 183 GHz of precipitation in Tropical Storm Cora. *J. Appl. Meteor.*, **21**, 1137–1145.

Wilheit, T. T., A. T. C. Chang, M. S. V. Rao, E. B. Rodgers and J. S. Theon, 1977: A satellite technique for quantitatively mapping rainfall rates over the oceans. *J. Appl. Meteor.*, **16**, 551–560.

Wiscombe, W. J., 1980: Improved Mie scattering algorithms. *Appl. Optics*. **19**, 1505–1509.

Figure 1: The microphysical vertical profiles of the cloud water, rain, cloud ice, snow, and graupel densities for stage C, stage E, stage M, and stage D.

Figure 2: The temperature and relative humidity profiles for the four cloud stages.

Figure 3: The brightness temperature perturbations from clear air for the four stages and six parameterizations at (a) 6.0 GHz, (b) 10.69 GHz, (c) 18.7 GHz, (d) 23.8 GHz, (e) 36.5 GHz, (f) 89.0 GHz, (g) 150.0 GHz, (h) 183.31+7.0 GHz, (i) 220.0 GHz, (j) 325.153+8.5 GHZ, (k) 340 GHz, and (l) 410.0 GHz. The calculations for the various parameterizations are shown to the left of the dashed line, to the right are the minima and maxima of the observed CAMEX-3 $T_B$. The minimum perturbed observed values for the mature Fig. 3g is -184K and for Fig. 3i is -180K.

Table 1: Microphysical size distribution parameters.

| Hydrometeor type | $N_{0_h}$ ($cm^{-4}$) | $\rho_h$ ($g/cm^3$) | $\langle r \rangle$ (mm) | $\langle r \rangle_{max}$ (mm) |
|---|---|---|---|---|
| Rain (MP) | 0.08 | 1.0 | 0.10 | 4.48 |
| Dry snow | 0.04 | 0.1 | 0.09 | 5.94 |
| Dry graupel | 0.04 | 0.4 | 0.11 | 5.88 |

Table 2: The six microphysical cloud parameterizations.

| Case | Description |
|---|---|
| 1 | Five hydrometeor phase model (baseline) with suspended cloud water, rain, suspended cloud ice (100% ice), dry snow (10% ice, 90%air), and dry graupel (40%ice, 60% air). Particle size distributions are provided in Table 1. |
| 2 | Five phase but with rain having a Joss et al. (1968) thunderstorm size distribution. This size distribution uses $N_{r0} = 0.014$ $cm^{-4}$ and $\Lambda_r = 14.49 M^{-0.249}$ $cm^{-1}$ in Eq. 3. |
| 3 | Five phase but with snow and graupel having a Sekhon and Srivastava (1970) (SS) size distribution, where $N_{s,g} = 6.4 \times 10^{-3} M^{-1.09}$ $cm^{-4}$ and $\Lambda_{s,g} = 11.9 M^{-0.52}$ $cm^{-1}$. |
| 4 | Five phase but with the ice-air-water ratio of snow being 20-80-0% and the ice-air-water ratio of graupel being 80-20-0%. |
| 5 | Five phase but with snow and graupel having liquid percentages as a function of temperature: for $T \leq 258.15$ K wetness $W = 0.0\%$, for $T > 273.15$ K, $W = 15\%$ and a linear interpolation of $W$ between 258.15 and 273.15 K. |
| 6 | Two phase with all liquid summed as MP rain and all frozen hydrometeors summed as SS ice. |

Table 3: Surface rain rates and integrated ice contents for the four storm stages.

| Stage | Rain Rate (mm/hr) | Integrated Ice Content ($kg/m^2$) | Approximate Stage | Symbol |
|---|---|---|---|---|
| C | 10.0742 | 0.5884 | Cumulus | × |
| E | 80.7251 | 7.6733 | Evolving | □ |
| M | 111.3941 | 28.9451 | Mature | ○ |
| D | 50.5127 | 17.6868 | Dissipating | △ |

Table 4: Frequency versus parameterization comparison. Stages with less than a 5 K difference from the baseline five-phase parameterization are indicated by blanks.

| Freq. (GHz) | Parameterization 2 | 3 | 4 | 5 | 6 |
|---|---|---|---|---|---|
| 6.0 | +CEMD | | | +EMD | +C, -M |
| 10.69 | +CD, -M | | -EMD | -M | +C, -EMD |
| 18.7 | +C, -ED | +MD | -EMD | | +C, -EMD |
| 23.8 | | +EMD | -EMD | +D | +C, -EMD |
| 36.5 | -C | +EMD | -CEMD | +EMD | -CEMD |
| 89.0 | | +CEMD | -CEMD | +EMD | -CEMD |
| 150.0 | | +CED | -CEMD | +ED | -CED |
| 183.31+7.0 | | +ED | -CEMD | +D | -CED |
| 220.0 | | +CED | -CEMD | +D | -CE |
| 325.15+8.5 | | +ED | -CEMD | +D | -CE |
| 340.0 | | +CED | -CEMD | | -CE |
| 410.0 | | +E | -CED | | CE |

Table 5: Summary of $T_B$ effects for various storm stages and parameterizations. Comparisons are with respect to parameterization 1.

| Stage | Parameterization | | | | |
|---|---|---|---|---|---|
| | 2 | 3 | 4 | 5 | 6 |
| Cumulus ($\times$) | a, b | f | i | m | s, t |
| Evolving ($\square$) | c, d | g | j | n, o, p | t |
| Mature ($\bigcirc$) | c, d | g, h | k | n, o, p, q | t, u |
| Dissipating ($\triangle$) | c, d | g | l | o, p, r | t, u |

Code Table

| Code | Effect/Interpretation |
|---|---|
| a | Joss rain PSD warms $T_B \leq 18.7$ GHz due to increased absorption for the larger drop. |
| b | The transition from warming due to the larger rain PSD to cooling due to liquid scattering occurs at 36.5 GHz. |
| c | The upper altitude particles reduce the probing depth at the higher frequencies. Warming due to the larger rain drop size is only seen at 6 GHz. |
| d | Same as **b**, but at 10.69 to 36.5 GHz depending on upper altitude hydrometeor content. |
| e | The SS smaller ice sizes warm all window channels $\geq 89$ GHz. |
| f | Same as **e** but for frequencies $\geq 18.7$ GHz due to additional ice in the profile. |
| g | For the mature stage and frequencies $\geq 150$ GHz ice scattering saturation occurs for the size distributions of both parameterizations 1 and 3. |
| h | Since stage C has little ice, doubling the ice ratio only affects $\geq 36.5$ GHz. |
| i | Doubling the ice ratio increases scattering and reduces $T_B$ for frequencies $\geq 19.69$ GHz. |
| j | Stage C has a minimally-thin melting layer, therefore no significant $T_B$ changes. |
| k | Warming due to increased liquid water content for 36.5—150 GHz. |
| l | Cloud top ice hydrometeors cause saturation and produce nearly the same $T_B$ for stages E, M and frequencies $> 150$ GHz. |
| m | Cooling at 10.7 GHz because snow/graupel appear as large raindrops (see **b**). |
| n | Warming response is reduced above 89 GHz because the high altitude large ice particles preclude probing into the melting layer. |
| o | Same as **k** except for 6.0 GHz and 23.8—325 GHz. |
| p | Absorptive warming due to larger particles of the combined cloud water and rain. |
| q | Increase in cooling due to larger particles associated with the combined ice, snow, and graupel. |
| r | Scattering saturation causes no significant $T_B$ change at higher frequencies. |

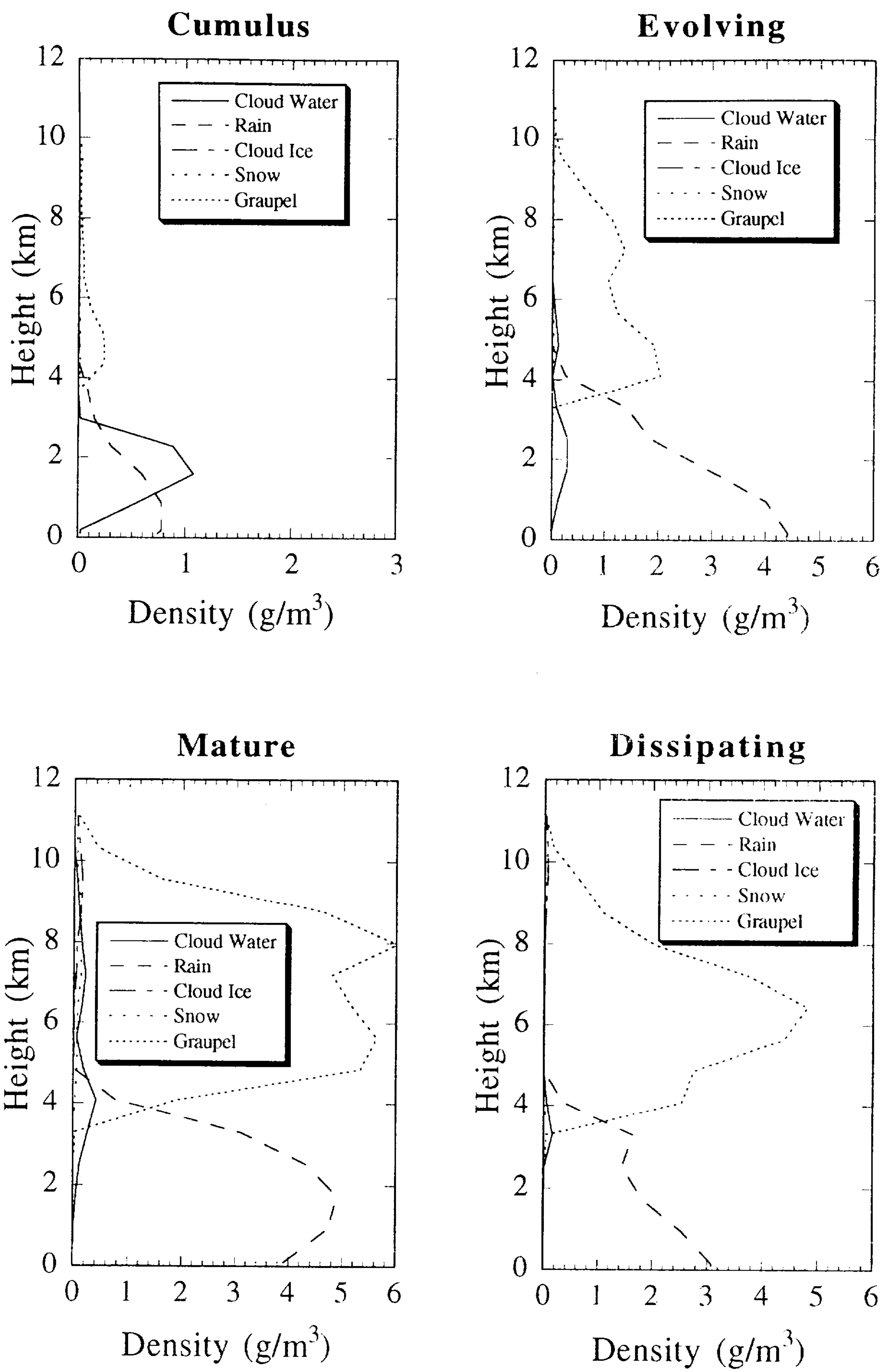


Skofronick-Jackson et. al. FIGURE 1

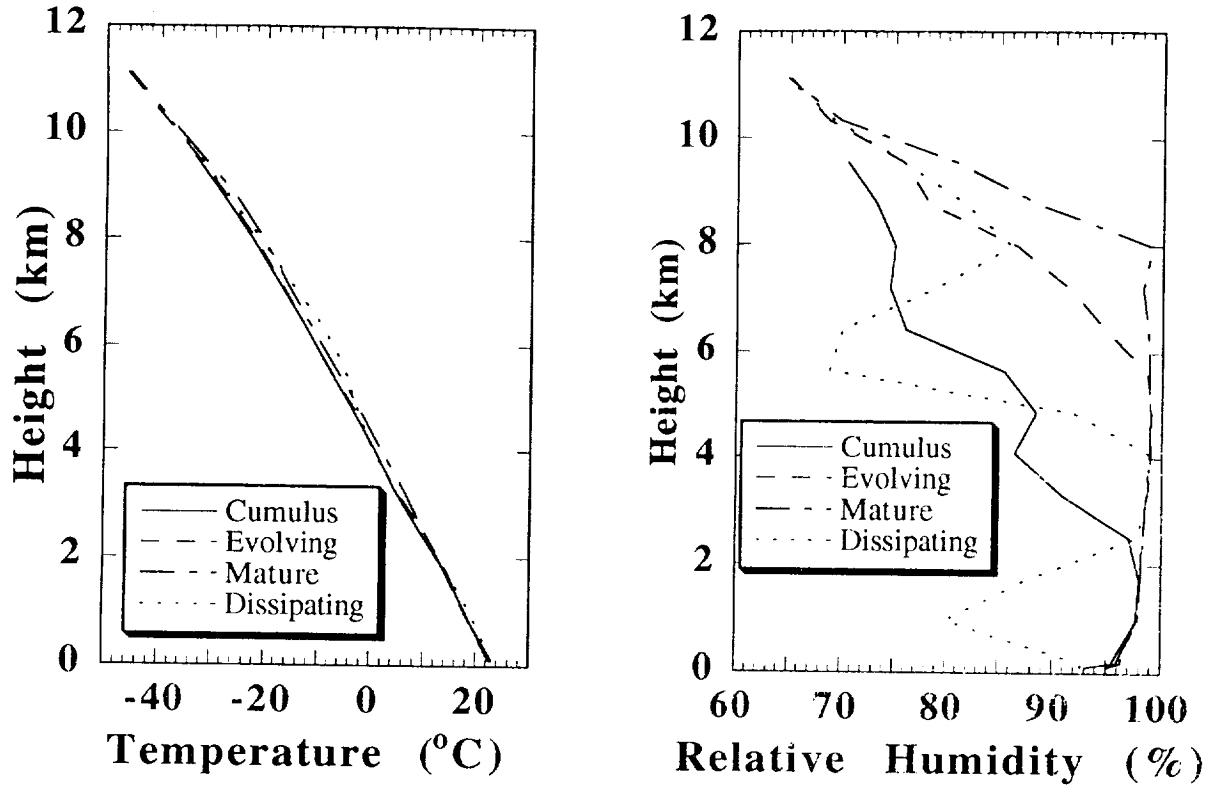


Skofronick-Jackson et. al. FIGURE 2

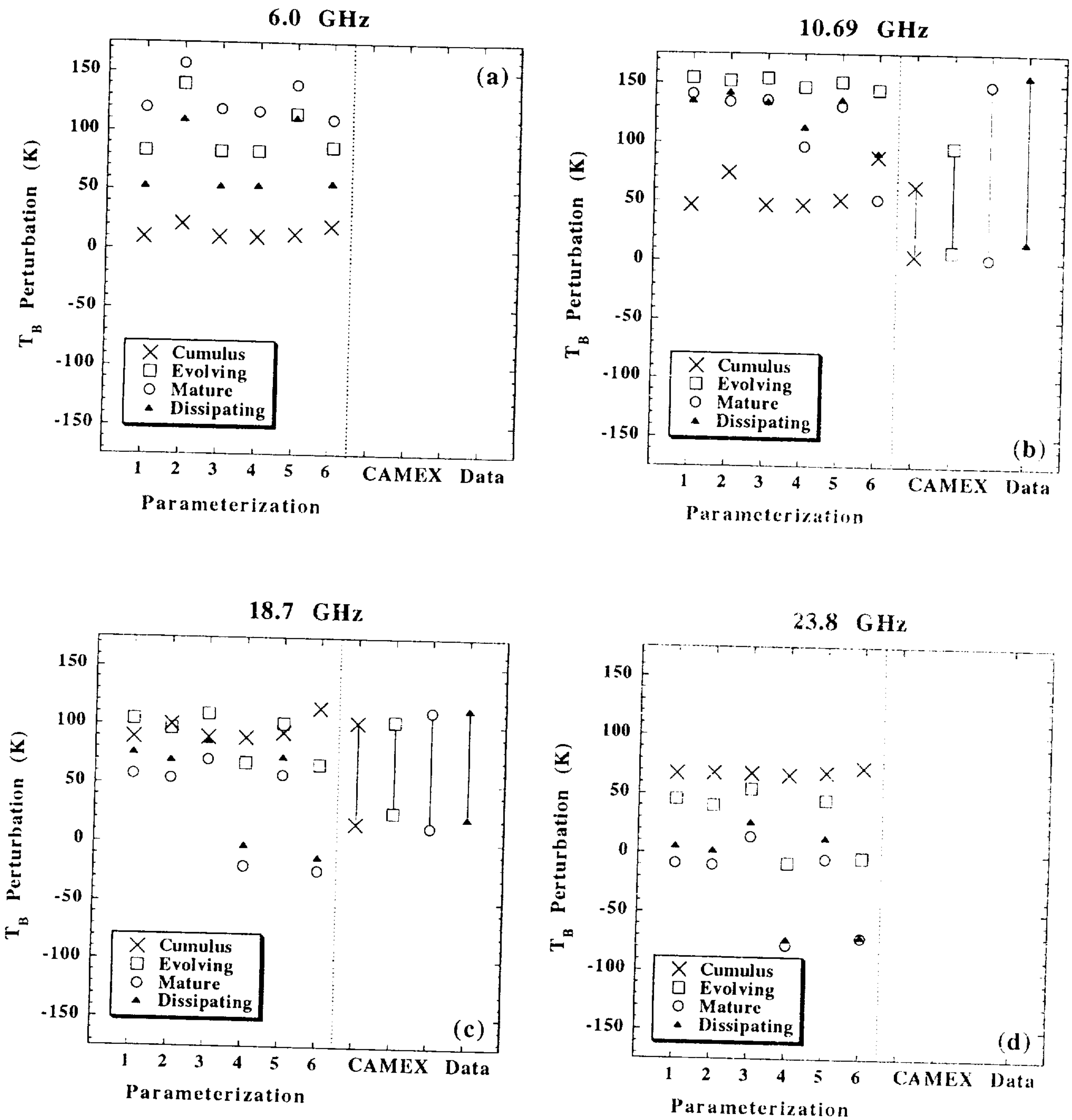


Skofronick-Jackson et. al. FIGURE 3

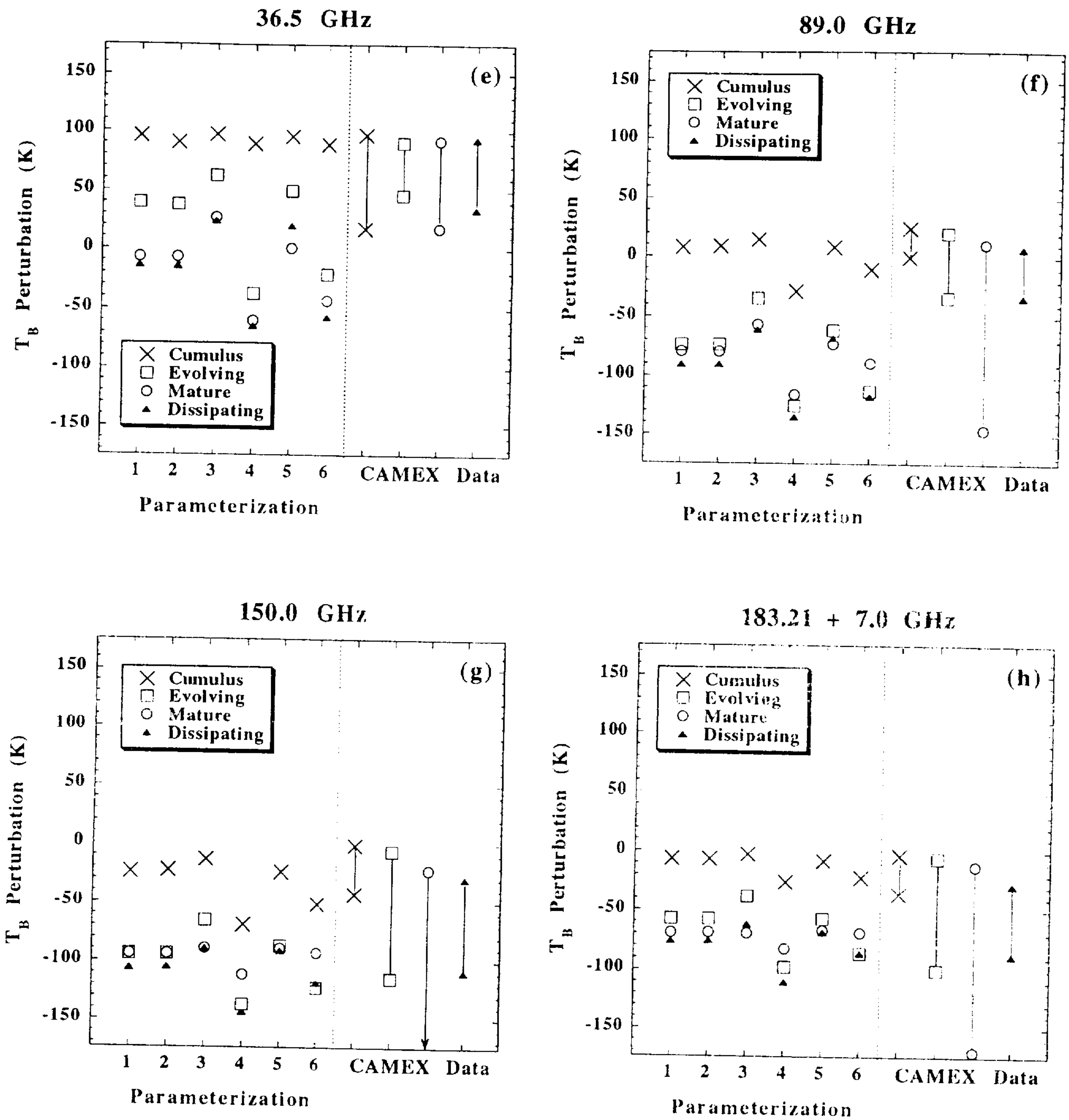


Skofronick-Jackson et. al. FIGURE 3

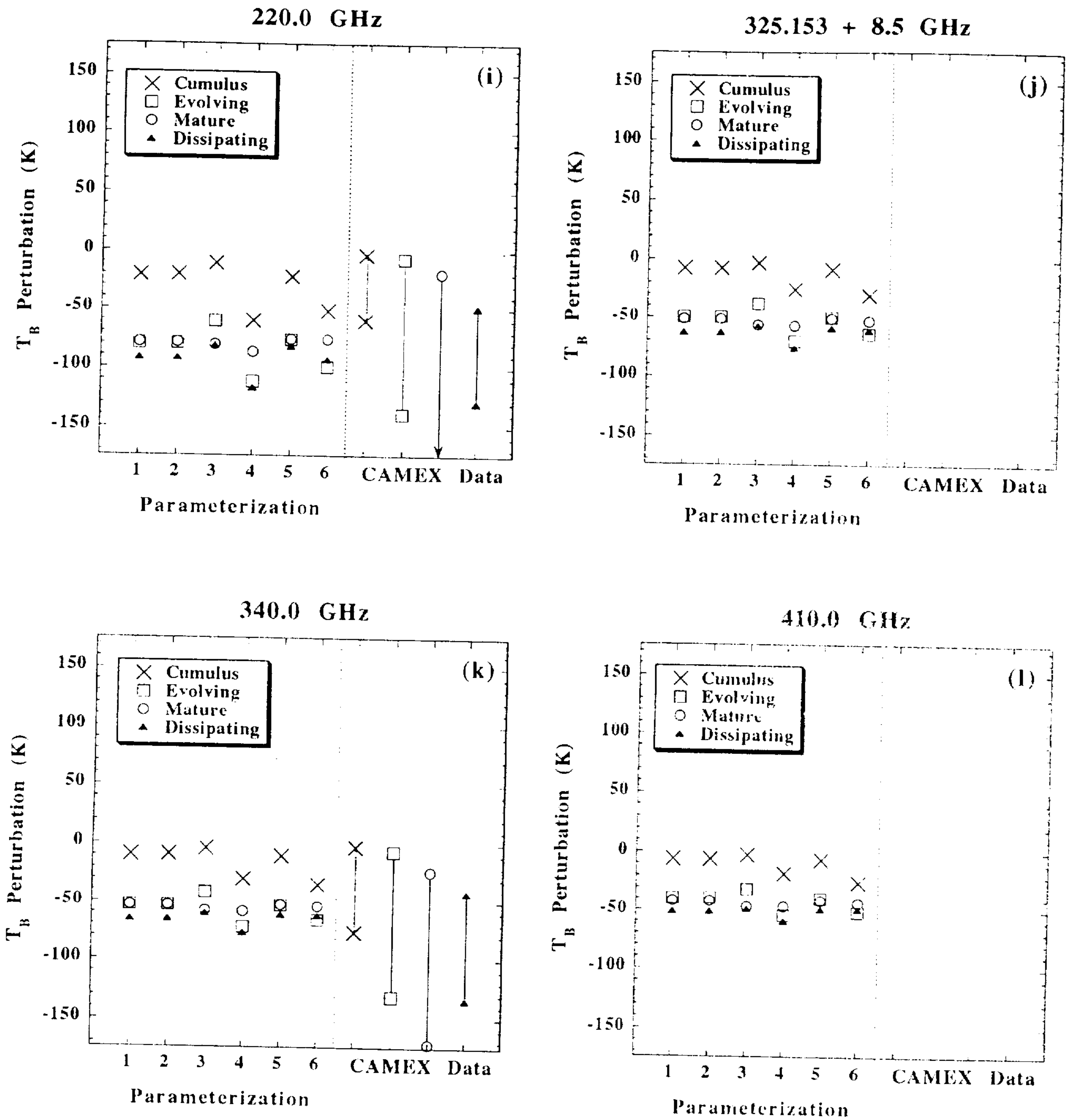


Skofroncik-Jackson et. al. FIGURE 3